ACS APPLIED MATERIALS & INTERFACES

www.acsami.org

Research Article

Flexible *n*-Type Abundant Chalcopyrite/PEDOT:PSS/Graphene Hybrid Film for Thermoelectric Device Utilizing Low-Grade Heat

Yanan Wang, Hong Pang,* Quansheng Guo, Naohito Tsujii, Takahiro Baba, Tetsuya Baba, and Takao Mori*

Cite This: *ACS Appl. Mater. Interfaces* 2021, 13, 51245−51254

Read Online

ACCESS | Metrics & More | Article Recommendations | Supporting Information

ABSTRACT: Combining inorganic thermoelectric (TE) materials with conductive polymers is one promising strategy to develop flexible thermoelectric (FTE) films and devices. As most inorganic materials tried up until now in FTE composites are composed of scarce or toxic elements, and *n*-type FTE materials are particularly desired, we combined the abundant, inexpensive, nontoxic Zn-doped chalcopyrite ($Cu_{1-x}Zn_xFeS_2$, x = 0.01, 0.02, 0.03) with a flexible electrical network constituted by poly(3,4-ethylenedioxythiophene) polystyrenesulfonate (PEDOT:PSS) and graphene for *n*-type FTE films. Hybrid films from the custom design of binary $Cu_{1-x}Zn_xFeS_2$/PEDOT:PSS to the optimum design of ternary $Cu_{0.98}Zn_{0.02}FeS_2$/PEDOT:PSS/graphene are characterized. Compared with the binary film, a 4-fold enhancement in electrical conductivity was observed in the ternary film, leading to a maximum power factor of ∼ 23.7 μW m^{-1} K^{-2}. The optimum ternary film could preserve >80% of the electrical conductivity after 2000 bending cycles, exhibiting an exceptional flexibility due to the network constructed by PEDOT:PSS and graphene. A five-leg thermoelectric prototype made of optimum films generated a voltage of 4.8 mV with a ΔT of 13 °C. Such an evolution of an inexpensive chalcopyrite-based hybrid film with outstanding flexibility exhibits the potential for cost-sensitive FTE applications.

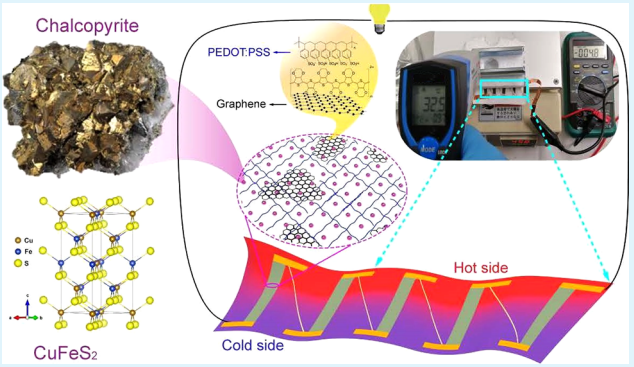

KEYWORDS: *n-type, chalcopyrite, PEDOT:PSS, graphene, flexibility, thermoelectric*

1. INTRODUCTION

With the transition of many electronic devices from traditionally rigid to flexible as well as wearable and implantable, the demand for a corresponding power supply, especially those that are autonomous with a long life, is growing.[1,2] Thermoelectric (TE) materials that can stably and directly convert ubiquitous heat or industrial waste heat into electric energy have become a hot topic in recent decades,[3−6] and especially now for their applicable potential in flexible TE (FTE) devices that can present conformal interactions with heat sources to maximize heat harvesting.[7−9] The energy conversion efficiency of TE materials is determined by a dimensionless figure of merit ZT ($ZT = S^2\sigma T\kappa^{-1}$), where S is the Seebeck coefficient, σ is the electrical conductivity, T is the working temperature and κ is the thermal conductivity, respectively. The combined parameter of $S^2\sigma$, called the power factor (PF), is an indicator of the maximum output power.[10] Until now, state-of-the-art TE materials with high ZT have been mostly inorganic bulk materials.[11,12]

Inorganic materials are typically rigid, and the focus of the research on FTE materials has been on conducting polymers (CPs) and CP-based composites.[13−18] Although the PF and ZT of CPs and CP-based composite materials are lower compared to inorganic TE materials, their flexibility and in principle low-cost device synthesis processes are the attraction. CPs typically have low thermal conductivity, so the challenge has been to improve the PF.[14,19,20] CP-related are mainly *p*-type so there has much effort devoted to developing *n*-type FTE materials.[21,22]

One strategy is incorporating inorganic TE materials like Ag_2Se, which have some flexibility themselves on various flexible polymer substrates including nylon,[23] polyimide,[24,25] copy paper,[26] silk,[27] etc. Nevertheless, it is observed that the TE properties have an apparently decrease as a result of microcracks caused by the increase in bending times in the film. Incorporating inorganic TE components into conductive polymer matrixes has been another effective strategy, trying to take advantage of the inherently low κ and good flexibility of conductive polymers and the superior charge transport

Received: August 10, 2021
Accepted: October 8, 2021
Published: October 22, 2021

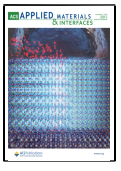

Scheme 1. Fabrication of the $Cu_{0.98}Zn_{0.02}FeS_2$/PEDOT:PSS/Graphene Film Supported by PTFE Membrane and Its Optical Photo

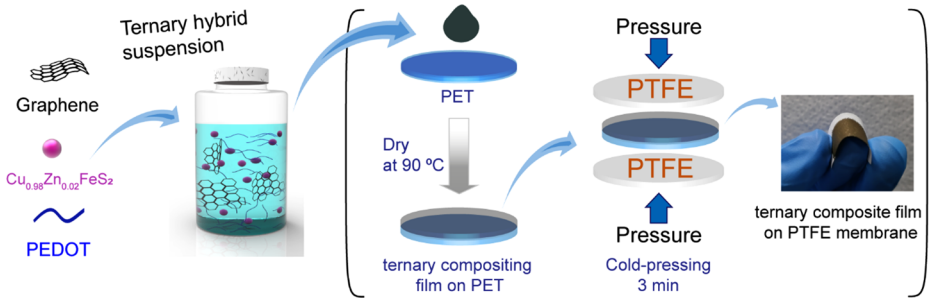

properties of inorganic components.[8,28] So far, poly(3,4-ethylenedioxythiophene) polystyrenesulfonate (PEDOT:PSS) has been widely studied as the polymer matrix in FTE composites because of its promising σ of 4380 S/cm at RT, stability in the air, robust mechanical properties, and commercialization.[29] Many groups have reported PEDOT:PSS-related FTE films with high performance and excellent flexibility.[30−35] For example, Goo et al.[30] prepared flexible proton-irradiated Bi_2Te_3/PEDOT:PSS composite films by a drop-casting method and obtained a maximum PF of 325.3 μW m^{-1} K^{-2} at RT, which is among the top values of Bi_2Te_3/PEDOT:PSS composites. More recently, Meng et al.[35] prepared a PEDOT:PSS/Ag_2Te composite film supported by poly(ether sulfone) (PES) membrane with a *PF* of 143.3 μW m^{-1} K^{-2} at RT, presenting a good flexibility. Although such new classes of relatively high-performance FTE films have emerged, most of them have as main constituents the scarce Te or toxic Se element, and/or expensive Ag element, which are not conducive to the requirements of low cost, environmental friendliness, and low toxicity for industrial application. In this work, instead of aiming for just high performance, we have tried to develop an FTE composite based on abundant, inexpensive, and ecofriendly inorganic materials.

One compelling TE inorganic material is nontoxic chalcopyrite, $CuFeS_2$,[36−39] which is composed of very cheap and abundant elements in the earth crust, and is a stable material free of any noticeable ionic conduction. Chalcopyrite has been widely studied as a potential *n*-type TE material, with its diamond-like structure contributing to intrinsically low lattice thermal conductivity, tetrahedrally bonding exhibiting large mobility,[40] and magnetism found to contribute to a large power factor at room temperature.[36,37]

Herein, based on the polytetrafluoroethylene (PTFE) membrane, *n*-type flexible thermoelectric composite films consisting of $Cu_{1-x}Zn_xFeS_2$ (x = 0.01, 0.02, 0.03), PEDOT:PSS were prepared by a drop-casting method combined with cold-pressing. The PEDOT:PSS forms an electrical network and provide flexibility to the composite films while the neighbor $Cu_{1-x}Zn_xFeS_2$ particles are bridged by the PEDOT:PSS to generate *n*-type conductivity of the films. Later we have strategically introduced graphene to optimize the interfacial carrier transports in $Cu_{1-x}Zn_xFeS_2$/PEDOT:PSS composite. It is found that σ, S, and PF of composite films exhibit a spike at a certain chalcopyrite mass fraction. Furthermore, the electrical conductivity and the mechanical flexibility of the composite films is improved with the assistance of graphene. The TE properties of the hybrid films are discussed and a prototype TE device based on the abundant mineral-based hybrid material is further demonstrated.

2. EXPERIMENTAL SECTION

2.1. Materials. Analytical grade elemental powders of Cu (99.7%), Zn (99.9%), and FeS_2 (99.8%) were purchased from Sigma-Aldrich. PEDOT:PSS solution (Heraeus Clevios TM PEDOT:PSS PH1000, 1.0−1.3 wt % in water) was obtained from As One. Ethanol (C_2H_5OH, 98%) was purchased from Wako chemicals. Dimethyl sulfoxide (DMSO), graphene nanoplatelets (6−8 nm thick ×15 μm wide), polyethylene terephthalate (PET, 0.013 mm in thickness), glass slides and polytetrafluoroethylene (PTFE) membrane (0.025 μm pore size, 25 mm in diameter) were purchased from Sigma-Aldrich. All the chemicals were of analytical grade.

2.2. Preparation of Chalcopyrite Powder. Zn-doped chalcopyrite were synthesized by the solid-state reaction method. High-purity powders of Cu (99.7%), Zn (99.9%), and FeS_2 (99.8%) were weighed and mixed in the stoichiometric proportions of $Cu_{1-x}Zn_xFeS_2$ (x = 0.01, 0.02, 0.03), specified in each section. The mixture powders were loaded into a quartz tube (diameter of 10 mm) which was sealed until the vacuum pressure was less than 2 × 10^{-3} mbar. These ampules were put vertically into a programmable resistance box furnace annealed at 973 K for 72 h. The obtained ingots were ground into rough powder in a glovebox under Ar atmosphere and sealed into the vacuum tube and annealed at 973 K for 72 h again. The final ingots were ball milled for 2 h by the 8000D Mixer/Mill and the milled powders were sieved to filter out large particles (>75 μm) in a glovebox.

2.3. Fabrication of the Binary Chalcopyrite/PEDOT:PSS and Ternary Chalcopyrite/PEDOT:PSS/Graphene Films. The fabrication process is similar to the previous report,[26] which was schematically depicted in Scheme 1. For the binary films, in a typical fabrication process, a specific amount (20 mg) of the as-synthesized chalcopyrite powder was well dispersed into a mixture solution constituted by 200 μL of PEDOT:PSS, 200 μL of ethanol, and 100 μL of distilled water, which were subjected to a vortex mixer for 5 min, followed by 0.5 h of ultrasonication. Aqueous PEDOT:PSS solution was first treated with 10 vol % polar solvent DMSO to improve the electrical conductivity.[41] PET substrates were precleaned by O_2 plasma for increasing the surface hydrophilicity. The mixture was then drop-casted on the PET substrate, which is fixed by a vacuum filter holder. The drop-casting sample was kept in an oven at 90 °C for 1 h to slowly remove the solvent. After the drop-casting and drying process, the composite film was dried and adhered onto the PET substrate. Subsequently, the PET-based binary film was sandwiched by two pieces of PTFE membranes and cold-pressed at 20 MPa for 3 min. After cold-pressing, the composite film was transferred from PET to the PTFE membrane because of a larger adhesion between the composite film and PTFE membrane. The same fabrication process was repeated for the films with 30, 40, and 50 mg $Cu_{1-x}Zn_xFeS_2$ (x = 0.01, 0.02, 0.03) powder. All the properties were measured using the PTFE-based composite films.

For the ternary films, prior to the fabrication process above, chalcopyrite powder and graphene nanoplatelets were first ball-milled

https://doi.org/10.1021/acsami.1c15232
ACS Appl. Mater. Interfaces 2021, 13, 51245−51254

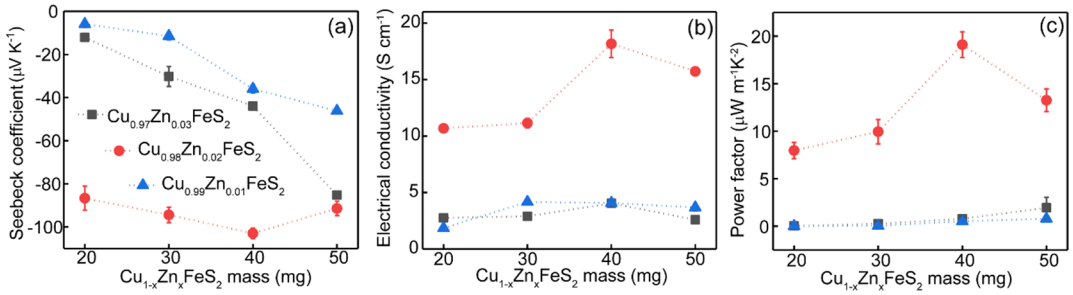

Figure 1. (a) Seebeck coefficient, (b) electrical conductivity, and (c) power factor of $Cu_{1-x}Zn_xFeS_2$/PEDOT:PSS binary films as the function of $Cu_{1-x}Zn_xFeS_2$ mass fraction (x = 0.01, 0.02, 0.03).

for 2 h to get graphene homogeneously dispersed in mixture. Four mass ratios of 20:1, 30:1, 40:1, and 50:1 between chalcopyrite and graphene nanoplatelets were prepared for the further compositing. The rest procedure to prepare ternary films is then the same as aforementioned in the binary film fabrication.

2.4. Measurement and Characterization. The microstructure and elemental distribution were observed using a field-emission scanning electron microscope (FE-SEM, Hitachi S-4800) equipped with an energy-dispersive spectrometer (EDS, Horiba EMAX Evolution X-Max 80). The crystallographic structure of the as-prepared composite materials was determined using Cu Kα radiation by RINT TTR-3 diffractometer (Rigaku Co., Akishima, Tokyo, Japan). The electrical conductivity and Seebeck coefficient values were obtained simultaneously using a commercial instrument (ZEM-3, Advance Riko). The measurement was carried out in a standard four-probe configuration under a helium atmosphere at RT. Raman spectrum were acquired on a HORIBA-Jobin-Yvon Micro Raman Spectrometer T64000. UV−vis absorption spectra were converted from the diffuse reflectance spectra collected on a UV−vis-NIR Spectrometer V-770 (JASCO). Hall mobility and carrier concentration was measured on ResiTest 8300 Series (Toyo Technica). The thermal conductivity was evaluated by (1) a picosecond time-domain thermoreflectance (TD-TR) method under a front-face heating front-face detection (FF) configuration with a PicoTR (Picotherm Corp) thermoreflectance apparatus. The wavelength of the pump beam is 1550 nm and that of the probe beam is 775 nm. The diameter of the pump beam focused on the sample is 45 μm and that of the probe beam is 25 μm. A 100 nm platinum layer was deposited on the films by DC sputtering system to detect thermoreflectance signals. The thermal conductivity was also evaluated by (2) ai-Phase Co., Ltd., which has developed a thermal diffusivity measurement apparatus of films by a front-face sinusoidal Joule heating and rear-face temperature detection method.

3. RESULTS AND DISCUSSION

The synthesized $Cu_{1-x}Zn_xFeS_2$ (x = 0.01, 0.02, 0.03) powder were characterized by XRD as seen in Figure S1. The TE properties of the binary films with 5−15 mg $Cu_{1-x}Zn_xFeS_2$ powder are shown in Figure S2. As a small amount of inorganic powder will introduce the p-type conducting feature into the compositing films, a mass range of 20−50 mg was chosen for optimizing the best content of inorganic proportion for the binary film. The S, σ, and PF of $Cu_{1-x}Zn_xFeS_2$/PEDOT:PSS (x = 0.01, 0.02, 0.03) were compared in Figure 1a−c. The negative S indicates that the composite films are n-type. Evidently, the film with x = 0.02 exhibits the highest TE properties at the different mass fractions. Hereafter, $Cu_{0.98}Zn_{0.02}FeS_2$ was selected as the inorganic matrix for all the composite films. According to the semiclassical Mott relation,[42] the effective S of the composite film should be compromised when compositing p-type polymers and n-type inorganic materials. However, the $Cu_{0.98}Zn_{0.02}FeS_2$/PEDOT:PSS film in this work still has an S (−102.5 μV/K) value that is competitive with the reported one (see Table S1), whereas the σ is extremely poor.

Figure 2a, b presents the microstructure of $Cu_{0.98}Zn_{0.02}FeS_2$ powder and the composite binary film at a 30 mg fraction,

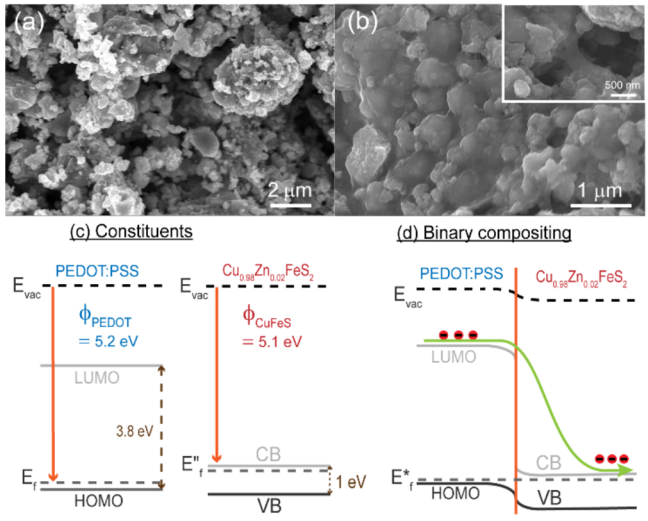

Figure 2. SEM image of (a) ball-milled $Cu_{0.98}Zn_{0.02}FeS_2$ powder and (b) binary film with 30 mg of $Cu_{0.98}Zn_{0.02}FeS_2$ (inset is the magnified image of the binary film). (c) Band diagram of the constituents; (d) band alignment between PEDOT:PSS and $Cu_{0.98}Zn_{0.02}FeS_2$.

respectively. The statistic average size of chalcopyrite is 514 ± 273 nm (see Figure S3). Compared to Figure 2a, even though the gaps between $Cu_{0.98}Zn_{0.02}FeS_2$ particles were stitched by PEDOT:PSS conductive paths, which facilitates the hopping movement of charge carriers between particles, the pores and bulges observed in Figure 2b negatively affect the effective conductivity of the composite film. On the other hand, according to the UV−vis absorption spectra in Figure S4, the bandgap of the $Cu_{0.98}Zn_{0.02}FeS_2$ and PEDOT:PSS is determined to be 1.0 and 3.8 eV, respectively. Referring to the literature, the work function of $Cu_{0.98}Zn_{0.02}FeS_2$ and PEDOT:PSS is 5.15 and 5.2 eV.[43−45] Accordingly, the conduction band (CB) position of the p-type PEDOT:PSS is estimated to locate near 1.4 eV with regards to the vacuum level, whereas the CB of the as-synthesized n-type $Cu_{0.98}Zn_{0.02}FeS_2$ is around 5.1 eV. As a result, the band diagrams of the PEDOT:PSS and $Cu_{0.98}Zn_{0.02}FeS_2$ are depicted in Figure 2c. The energy alignment (P−N junction) in Figure 2d explains the poor electrical conductivity due to the electron−hole pair recombination at the P−N junction,

https://doi.org/10.1021/acsami.1c15232
ACS Appl. Mater. Interfaces 2021, 13, 51245−51254

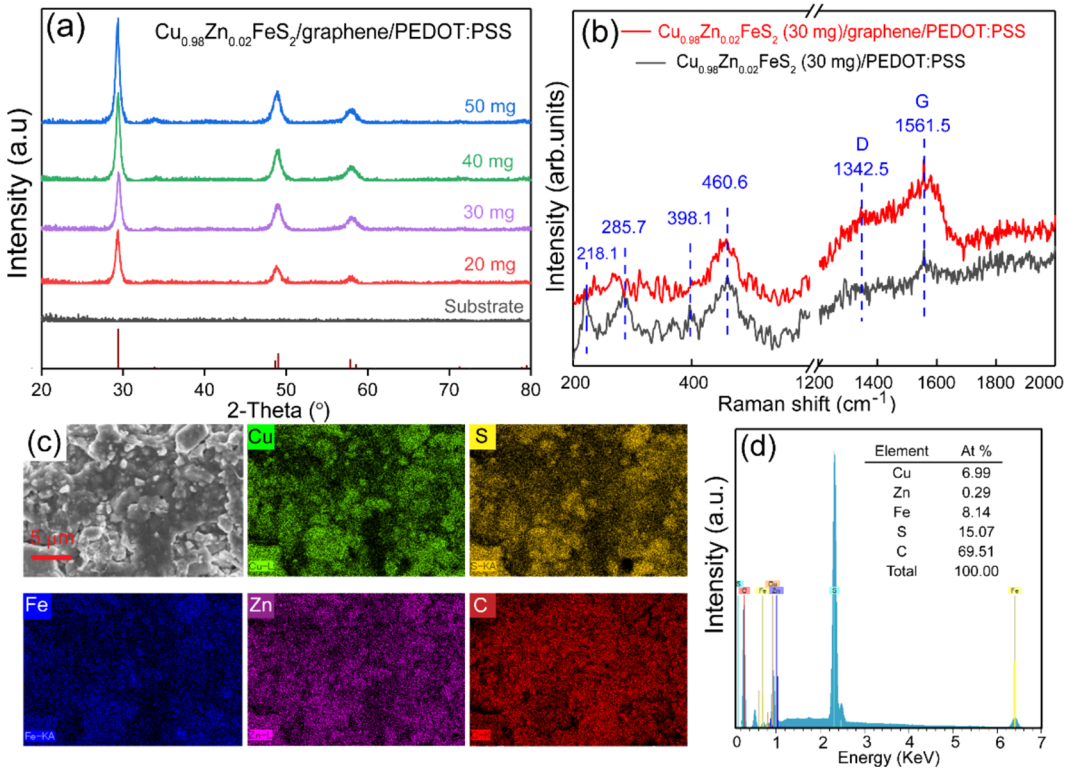

Figure 3. Characterization of the ternary films: (a) XRD patterns with different $Cu_{0.98}Zn_{0.02}FeS_2$ mass; (b) Raman spectra of the ternary and binary film at 30 mg fraction; (c) EDX mapping (the scale bar of all the mappings is 5 μm) and (d) spectra and composition of the ternary film at a 30 mg fraction.

which compromises the carrier concentration and thus suppresses σ. Ultimately, a modest PF of 19.1 $\mu W\ m^{-1}\ K^{-2}$ was obtained from $Cu_{0.98}Zn_{0.02}FeS_2$(40 mg)/PEDOT:PSS.

Taking into account that the electrical conductivity of inorganic materials will decrease when they are reduced in dimensionality and that the interfacial contact resistance is relatively high when incorporating them into the conductive polymer, many researchers have tried to address it by adding carbon allotropes.[8,10,46−52] The significant enhancement of the PF was observed because of the enhanced σ caused by the optimized carrier concentration and/or reduced void volume fraction between inorganic particles. Among these carbon allotropes, graphene, a one-atom-thick sp^2-bonded planar carbon sheet, has frequently been considered as a promising filler to construct better conducting channels because of its higher theoretical surface area, high electrical conductivity, stable thermal properties, and excellent mechanical and chemical properties. Moreover, it has been reported that the $\pi-\pi$ interaction between PEDOT:PSS and graphene ordered the PEDOT:PSS molecular chain arrangement and conversely made graphene disperse more homogeneously in the matrix, leading to an increase in carrier mobility and electrical conductivity.[53−55] Herein, graphene nanoplatelets were introduced to the binary $Cu_{0.98}Zn_{0.02}FeS_2$/PEDOT:PSS films.

The XRD patterns of $Cu_{0.98}Zn_{0.02}FeS_2$/PEDOT:PSS/graphene (20−50 mg/200 μL/1 mg) hybrid films were first measured and shown in Figure 3a. Only $Cu_{0.98}Zn_{0.02}FeS_2$ diffraction peaks were discernible, implying the stability of the $Cu_{0.98}Zn_{0.02}FeS_2$ during the solution treatment. The peaks for graphitic structure were not observed because of the small amount of graphene; there is also no characteristic peak of PEDOT:PSS because of its amorphous crystal structure. To prove the existence of graphene and its interaction with the matrix, the Raman spectra of binary and ternary films were performed, as shown in Figure 3b. The characteristic peaks of chalcopyrite at around 218.1, 285.7 (A_1 modes), 398.1 (B_2 modes), and 460.6 cm^{-1} (E modes) were observed in both composite films. In ternary film, excepting the peaks of chalcopyrite, the characteristic D (~1350 cm^{-1}) and G bands (~1585 cm^{-1}) of graphene are observed, which are related to the vibrations of sp^3-type disordered, activated carbon atoms and the sp^2-like carbon atoms, respectively.[56] A discernible decreased intensity of Raman peaks at 218.1 cm^{-1}, caused by the surface optical vibration, was observed in the ternary film, indicating the relaxation of the surface strain after the interaction between $Cu_{0.98}Zn_{0.02}FeS_2$ and graphene.[50,51,57] Figure 3c , d give the SEM-EDX analysis and the corresponding energy-dispersive X-ray spectroscopy of the ternary film. The mapping result confirmed that Cu, Zn, Fe, S, and C elements are uniformly distributed in the composite film. The EDX of $Cu_{0.98}Zn_{0.02}FeS_2$ and $Cu_{0.98}Zn_{0.02}FeS_2$/graphene powder is shown in Figure S5. The semi-quantification from EDX spectrum indicates that the composition of the ternary film is Cu, Zn, Fe, S, and C. The composition of Cu:Zn:Fe:S is approximately 23:1:27:49, which is close to the nominal composition of $Cu_{0.98}Zn_{0.02}FeS_2$. The thickness variation of ternary films (20, 30, 40, and 50 mg) can be seen in Figure S6.

As the PEDOT:PSS amount is correlated with the chalcopyrite amount as indicated in the binary films, to optimize the TE properties of ternary films, we mainly optimized the graphene mass and chalcopyrite powder. By compositing the 30 mg $Cu_{0.98}Zn_{0.02}FeS_2$ with PEDOS:PSS and different amount of graphene, the optimal amount of graphene

https://doi.org/10.1021/acsami.1c15232
ACS Appl. Mater. Interfaces 2021, 13, 51245−51254

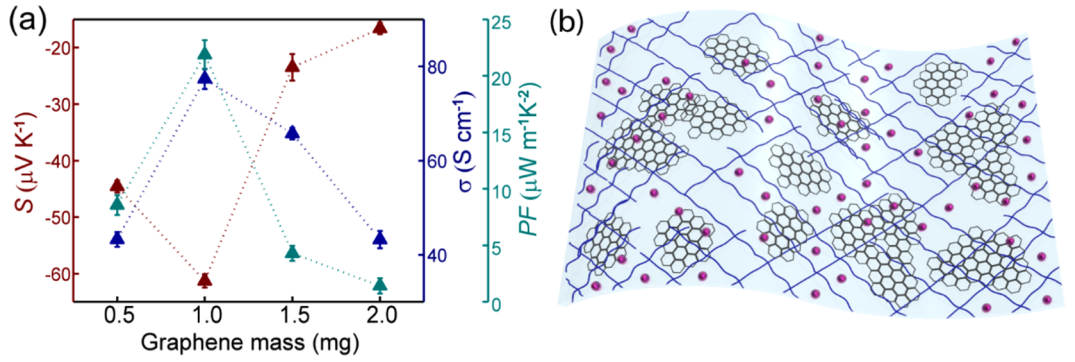

Figure 4. (a) Seebeck coefficient, electrical conductivity, and power factor of the $Cu_{0.98}Zn_{0.02}FeS_2$/PEDOT:PSS/graphene film as a function of graphene mass; (b) schematic illustration of the $Cu_{0.98}Zn_{0.02}FeS_2$/PEDOT:PSS/graphene film.

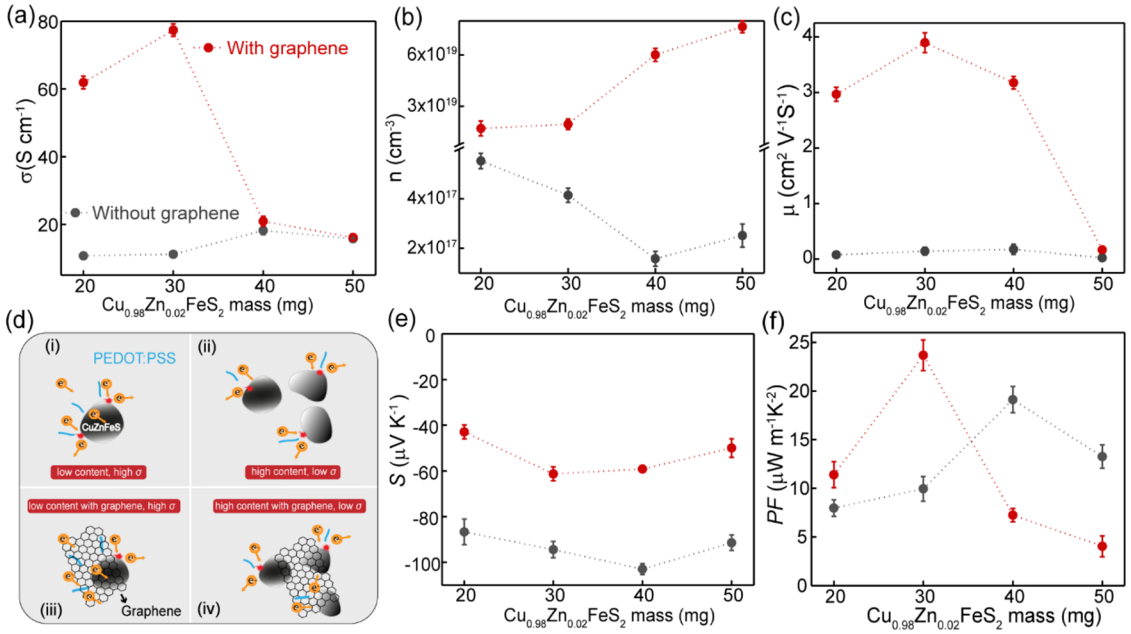

Figure 5. TE properties of binary and ternary film as a function of $Cu_{0.98}Zn_{0.02}FeS_2$ mass: (a) electrical conductivity, (b) carrier concentration, (c) carrier mobility, (d) schematic illustration of the carrier transport mechanism with (i, iii) low content and (ii, iv) high content of $Cu_{0.98}Zn_{0.02}FeS_2$, (e) Seebeck coefficient, and (f) power factor.

was assessed by TE properties of $Cu_{0.98}Zn_{0.02}FeS_2$/PEDOT:PSS/graphene (30 mg/200 μL/0.5−2.0 mg) film at RT. As shown in Figure 4a, 1 mg of graphene was evaluated as the optimal mass because the maximum σ, S, and PF were obtained at this fraction. The electrical conductivity of the ternary film at 1 mg (77.3 S cm^{-1}) was ~4.3 times higher than the maximum for the binary film (18.2 S cm^{-1}), which is ascribed to the intrinsically high conductivity of graphene. In regards to S, the negative S values indicate that the introduction of graphene does not alter the type of composite film. Although the S (−61.3 μV K^{-1}) value obtained with 1 mg of graphene is slightly compromised compared to the maximum S in the binary film, the higher PF (23.7 μW m^{-1} K^{-2}) was obtained in the ternary film with 1 mg of graphene.

As graphene mass increased from 0.5 to 1 mg, S and σ behaved in a similar increasing trend because of the potential barriers existing at the interfaces between $Cu_{0.98}Zn_{0.02}FeS_2$ and graphene. As the mass fraction of graphene is further increased, a rapidly decreasing trend is observed in the electrical conductivity and the Seebeck coefficient because the excessive graphene causes agglomeration in the matrix. When graphene nanosheets agglomerated within the matrix, the carrier mobility was destructed by the thicker graphene.[58,59] Meanwhile, more wrinkles formed on the surface of the graphene nanosheets as a result of agglomeration caused by strong van der Waals forces between graphene layers. Therefore, the $\pi-\pi$ conjugation interactions between the graphene and the polymer could be severely weakened, worsening the electrical transport and reducing Seebeck coefficients at the same time.[60,61] As schematically illustrated in Figure 4b, only an appropriate graphene mass is beneficial for building conductive networks in porous films to moderate the pore-related effect and enhance the FTE properties in turn.

Subsequently, we optimized the TE properties of ternary films through varying the $Cu_{0.98}Zn_{0.02}FeS_2$ mass fraction. Figure 5a shows electrical conductivity of binary and ternary films as a function of $Cu_{0.98}Zn_{0.02}FeS_2$ mass at 20, 30, 40, and 50 mg. When compared to binary film, the addition of highly conductive graphene substantially increased the effective σ of the ternary films especially at 30 mg fraction; as aforementioned, the maximum conductivity of ~77.4 S cm^{-1} is more than 4 times higher than that of the $Cu_{0.98}Zn_{0.02}FeS_2$/

https://doi.org/10.1021/acsami.1c15232
ACS Appl. Mater. Interfaces 2021, 13, 51245−51254

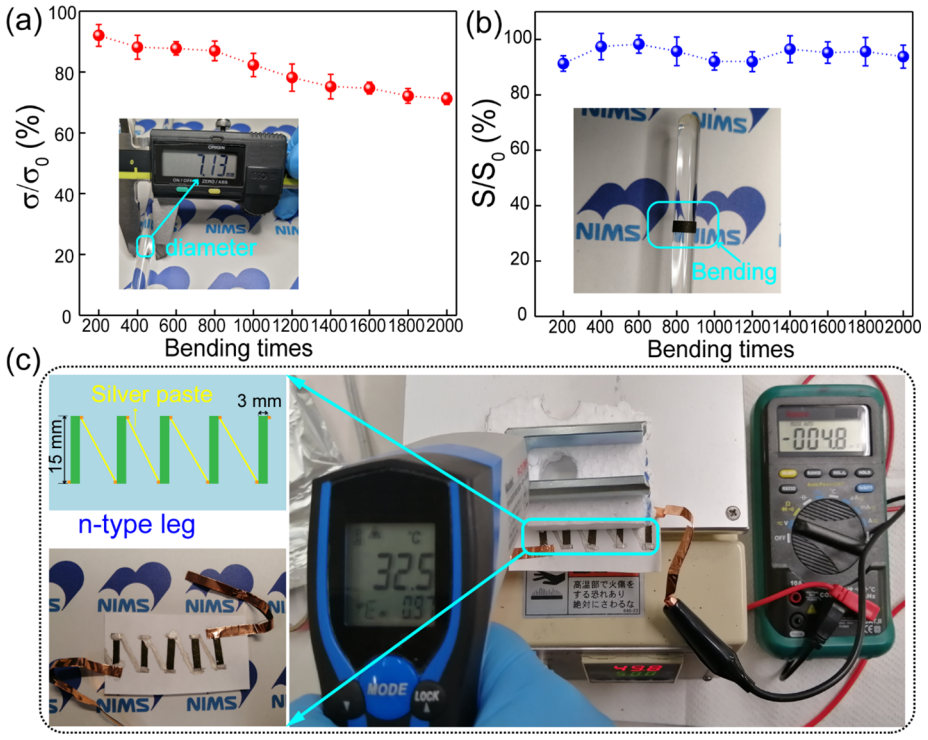

Figure 6. Relative rate of (a) electrical conductivity and (b) Seebeck coefficient. The inset in a shows the photo of a glass rod and that in b shows the bending of the $Cu_{0.98}Zn_{0.02}FeS_2$/PEDOT:PSS/graphene film around the rod. (c) Schematic diagram of a homemade FTE device (left-top), image of the as-fabricated FTE device (left-bottom), and its thermovoltage generation with heating plate (right) as thermal source.

PEDOT:PSS film (18.2 S cm^{-1}). To understand this phenomenon, the Hall-effect measurement was performed. It should be noted that samples for carrier concentration and mobility were prepared with glass substrates because the flexible films could be easily damaged by the probes of the particular Hall measurement. Accordingly, the rough data of carrier concentration (n) and carrier mobility (μ) of binary and ternary film are respectively shown in Figure 5b and c. The n and μ of the ternary films are significantly enhanced compared to those of the binary films over the mass fraction range originating from the "metallic" characterize of graphene and the additional net paths constructed by it, except for the μ at 50 mg ascribed to high contact resistance. Further increasing the $Cu_{0.98}Zn_{0.02}FeS_2$ mass, the deteriorated σ was obtained from the as-prepared films because of the relatively high interfacial contact resistance, which leads to the depressed μ and low σ (as listed in the Table S2).[30,62] The carrier transport mechanism is schematically drawn in Figure 5d. For low $Cu_{0.98}Zn_{0.02}FeS_2$ content (≤30 mg), the carriers in the binary film have to hop from one chalcopyrite to the neighboring chalcopyrite via PEDOT:PSS. With low chalcopyrite content (i), there are larger gaps between the two adjacent chalcopyrites, which is the predominant barrier affecting the σ. There are high path density and relative low porosity, which is converse in high $Cu_{0.98}Zn_{0.02}FeS_2$ content (>30 mg). The high content of chalcopyrite can fill in the gaps and shorten the distance that carriers hop as illustrated in (ii). Thus, there is slight improvement on the binary film when increasing the chalcopyrite amount. But the situation is different in the presence of graphene. At low chalcopyrite content (iii), the graphene can act as the carrier transport media with low electrical resistance, beneficial for the electrical conductivity improvement. However, the excessive content of chalcopyrite with graphene (iv) induces severe aggregation and much more interfaces, which is harmful for the carrier transport.

Figure 5e shows the S variation of binary and ternary films as a function of $Cu_{0.98}Zn_{0.02}FeS_2$ mass. The Seebeck coefficients of ternary films decreased a lot compared to those of binary films because of the enhanced conductivities. However, the degree of the Seebeck coefficient decrease was relatively low compared with the increased magnitude of carrier concentration, which is caused by the energy filtering effect. According to the diagram of the ternary hybrid in Figure S7b, when the graphene was implanted between the $Cu_{0.98}Zn_{0.02}FeS_2$ and PEDOT:PSS, the upward band bending of $Cu_{0.98}Zn_{0.02}FeS_2$ created the energy barriers at the interface between $Cu_{0.98}Zn_{0.02}FeS_2$ and graphene. The band offset was reflected by the flat band potential, which is calculated by the equation in Supporting Information Note I. Taking into account that graphene performs as a metal with infinite electrons, the flat band potential of the compositing film is close to the Fermi level (E_f) of graphene, which results in a positive ΔE after band alignment with $Cu_{0.98}Zn_{0.02}FeS_2$, as listed in Table S3, the E_{fb} of the ternary film with 30 mg of $Cu_{0.98}Zn_{0.02}FeS_2$ is larger than that with 20 mg, indicating a larger ΔE. The larger the ΔE, the more carriers with low energy are filtered, thus driving the average of carrier energy to a higher degree, leading to a higher Seebeck coefficient. As a result, combination of the maximum electrical conductivity and Seebeck coefficient yields a power factor as high as 23.7 μW m^{-1} K^{-2} for $Cu_{0.98}Zn_{0.02}FeS_2$(30 mg)/PEDOT:PSS/graphene at RT, as shown in Figure 5f.

The thermal conductivity of flexible ternary films was measured using the picosecond TD-TR method to obtain the local thermal conductivity κ at RT.[63] The κ values are in the range of 1.9~4.5 W m^{-1} K^{-1} for the ternary films. To confirm

https://doi.org/10.1021/acsami.1c15232
ACS Appl. Mater. Interfaces 2021, 13, 51245−51254

Table 1. Thermoelectric Voltage Generation of Flexible Thermoelectric Devices

		materials			
authors	methods	*n*	*p*	ΔT (K)	V_{oc} (mV)
Mallick et al.[65]	screen-printed	Ag_2Se	PEDOT:PSS	30	71.1
Lu et al.[47]	vacuum filtration	Ag_2Se/Ag/CuAgSe	Ag paste	18	5.2
Chen et al.[66]	drop-casting	Co NWs/PVDF	PEDOT:PSS	10	6.9
Tian et al.[67]	deposited method	TiS_2/organic films	PEDOT:PSS	70	33
Oh et al.[68]	vacuum filtration	WS_2	$NbSe_2$	3	2.4
Lu et al.[27]	depositing	Bi_2Te_3	Sb_2Te_3	35	10
Wan et al.[69]	solution synthesis	$TiS_2HA_{0.01}NMF_{0.003}$		20	1.3
This work	drop-casting	$Cu_{0.98}Zn_{0.02}FeS_2$/PEDOT: PSS/graphene	Ag paste	13	4.8

the obtained data, we evaluated the thermal conductivity of the whole films by a specialty measurement company, ai-Phase Co Ltd., by a front-face sinusoidal Joule heating and rear-face temperature detection method. In this case, the thermal diffusivity of the ternary film was determined to be 1.10−1.28 $mm^2\ s^{-1}$, leading to a κ = 2.4−2.8 W $m^{-1}\ K^{-1}$, which is consistent with the result from TD-TR. The relatively large ranges of the measured values might be attributed to the respective local nature of the measurement probes and inherent inhomogeneity of the composite samples. No significant difference in thermal conductivity between films with graphene (3.2 wt %) and without graphene could be observed, considering the relatively large scattering of measured values. In any case, the thermal conductivities of the composite films are indicated to be reduced compared to the bulk Zn doped chalcopyrite which was reported to have $\kappa \approx 7$ W $m^{-1}\ K^{-1}$ at RT.[36]

To examine the reliability of the $Cu_{0.98}Zn_{0.02}FeS_2$/PEDOT:PSS/graphene film (30 mg fraction), we applied a bending test around a glass rod with a diameter of 7.13 mm, and the relative rate of σ/σ_0 and S/S_0 (σ_0 and S_0 are the conductivity and the Seebeck coefficient before bending) were measured and are shown in Figure 6a, b. After 2000 cycles of bending measurements, the electrical conductivity decreased by no more than 25%, whereas the Seebeck coefficient does not have a significant change. The decrease in electrical conductivity was mainly caused by the microcracks, which became serious with increased bending times, as shown in Figure S8. These results show the excellent mechanical flexibility of the ternary film compared to the binary film, which descends sharply after 200 cycles of bending measurements, as shown in Figure S9. The network matrix from the synergic construction of PEDOT:PSS and graphene can effectively bridge the $Cu_{0.98}Zn_{0.02}FeS_2$ particles meanwhile significantly absorb the outer mechanical stress.

To make the $Cu_{0.98}Zn_{0.02}FeS_2$/PEDOT:PSS/graphene film into real applications, we fabricated a prototype power generator based on five legs of tailored $Cu_{0.98}Zn_{0.02}FeS_2$/PEDOT:PSS/graphene film. The length and width of each leg are 15 mm and 3 mm, respectively. Each leg was connected by silver paste and the prototype was supported by a piece of paper. The electrodes of the prototype device were connected by copper foils. To obtain the accurate temperature applied on the device, a temperature meter was used to measure the constant temperature field provided by a temperature controlling apparatus at hot side. The open-circuit voltage (V_{oc}) of the device was measured depending on the temperature differences between heating plate (32.5 °C) and air, as shown in Figure 6c (right). A V_{oc} value of 4.8 mV was obtained at a ΔT of 13 °C, which is compared with the previously reported TE devices, as listed in the Table 1. Therefore, the maximum output power can be estimated by using the formula $P_{max} = V_{oc}^2/4R_{in}$,[64] where R_{in} represents the internal resistance of the device. Here, the R_{in} is evaluated as 160 Ω. Accordingly, P_{max} was 36 nW when the temperature of the hot side was 32.5 °C. The comparison with the reported P_{max} is shown in Table S4. The result demonstrates that a flexible TE generator prototype made of $Cu_{0.98}Zn_{0.02}FeS_2$/PEDOT:PSS/graphene flexible films generates a respectable thermoelectric voltage from the low-grade heat. Although the Ag_2Se-based device has a higher output voltage of the generator,[65] there is room to further enhance the present $CuFeS_2$-based device performance after optimizing the material combinations and the device configuration. Furthermore, in terms of abundance, cost, stability, and nontoxicity, $CuFeS_2$ has a large prospective advantage compared to Ag_2Se, considering one of the important rationales for using such inorganic−polymer FTE composites to begin with is the low-cost device synthesis process.

4. CONCLUSION

In summary, we have rationally designed a ternary *n*-type flexible thermoelectric film composed of abundant mineral-based chalcopyrite $Cu_{0.98}Zn_{0.02}FeS_2$, PEDOT:PSS, and graphene. The processes to obtain optimized TE properties in such a system was developed. The optimum TE film demonstrates an enhanced electrical conductivity of ∼77.4 S cm^{-1} and a maximum power factor of ∼23.7 μW $m^{-1}\ K^{-2}$. Furthermore, the electrical conductivity and the Seebeck coefficient of the composite film retained more than 80% of their values after 2000 bending cycles, proving that the composite film is a promising candidate in the family of *n*-type FTE films. This work testified the feasibility of flexible composite TE films by implanting the inorganic TE materials into the polymer−graphene scaffolds, but the film could be improved through several ways in the future: (1) to synthesize the uniform TE nanocrystals and control the size via chemical synthesis; (2) to improve the dispersion of the nanofillers and avoid the undesirable agglomeration by capping the graphene with surfactants or grafting with functional groups. We believe our present work opens a possibility of nontoxic and low-cost flexible heat-harvesting generators, and the demonstrated successful fabrication will contribute to further rational design in three-component hybrids and boost the research related to such systems.

■ ASSOCIATED CONTENT

Supporting Information

The Supporting Information is available free of charge at https://pubs.acs.org/doi/10.1021/acsami.1c15232.

https://doi.org/10.1021/acsami.1c15232
ACS Appl. Mater. Interfaces 2021, 13, 51245−51254

XRD curves; TE properties curves; UV−vis absorption spectra; tables for TE and devices properties; SEM cross-section images; tables for carrier mobility and energy barriers; band diagram images; flexibility measurement curves (PDF)

AUTHOR INFORMATION

Corresponding Authors

Hong Pang − *International Center for Materials Nanoarchitectonics (WPI-MANA), National Institute for Materials Science (NIMS), Tsukuba 305-0044, Japan*; Email: PANG.Hong@nims.go.jp

Takao Mori − *International Center for Materials Nanoarchitectonics (WPI-MANA), National Institute for Materials Science (NIMS), Tsukuba 305-0044, Japan; Graduate School of Pure and Applied Sciences, Tsukuba University, Tsukuba 305-8671, Japan*; orcid.org/0000-0003-2682-1846; Email: MORI.Takao@nims.go.jp

Authors

Yanan Wang − *International Center for Materials Nanoarchitectonics (WPI-MANA), National Institute for Materials Science (NIMS), Tsukuba 305-0044, Japan; Graduate School of Pure and Applied Sciences, Tsukuba University, Tsukuba 305-8671, Japan*

Quansheng Guo − *International Center for Materials Nanoarchitectonics (WPI-MANA), National Institute for Materials Science (NIMS), Tsukuba 305-0044, Japan*

Naohito Tsujii − *International Center for Materials Nanoarchitectonics (WPI-MANA), National Institute for Materials Science (NIMS), Tsukuba 305-0044, Japan*; orcid.org/0000-0002-6181-5911

Takahiro Baba − *International Center for Materials Nanoarchitectonics (WPI-MANA), National Institute for Materials Science (NIMS), Tsukuba 305-0044, Japan*

Tetsuya Baba − *International Center for Materials Nanoarchitectonics (WPI-MANA), National Institute for Materials Science (NIMS), Tsukuba 305-0044, Japan*

Complete contact information is available at: https://pubs.acs.org/10.1021/acsami.1c15232

Author Contributions

Y.W., Q.G., and N.T. prepared and measured the sample. H.P. and T.M. conceived and directed the experiment. Ta.B. and Te.B. measured the sample. All authors have approved the final version of the manuscript.

Notes

The authors declare no competing financial interest.

ACKNOWLEDGMENTS

This work was supported by JST Mirai Program Grant JPMJMI19A1. Y.W. gratefully acknowledges financial support from the China Scholarship Council (CSC).

REFERENCES

(1) Mori, T.; Priya, S. Materials for Energy Harvesting: At the Forefront of A New Wave. *MRS Bull.* **2018**, *43* (3), 176−180.

(2) Dagdeviren, C.; Li, Z.; Wang, Z. Energy Harvesting from the Animal/Human Body for Self-Powered Electronics. *Annu. Rev. Biomed. Eng.* **2017**, *19*, 85−108.

(3) Bell, L. E. Cooling, Heating, Generating Power, and Recovering Waste Heat with Thermoelectric Systems. *Science* **2008**, *321*, 1457.

(4) He, J.; Tritt, T. M. Advances in Thermoelectric Materials Research: Looking Back and Moving Forward. *Science* **2017**, *357* (6358), 1369.

(5) Hong, S.; Gu, Y.; Seo, J. K.; Wang, J.; Liu, P.; Meng, Y. S.; Xu, S.; Chen, R. Wearable Thermoelectrics for Personalized Thermoregulation. *Sci. Adv.* **2019**, *5*, eaaw0536.

(6) Liu, Z.; Sato, N.; Gao, W.; Yubuta, K.; Kawamoto, N.; Mitome, M.; Kurashima, K.; Owada, Y.; Nagase, K.; Lee, C.-H.; Yi, J.; Tsuchiya, K.; Mori, T. Demonstration of Ultrahigh Thermoelectric Efficiency of ∼ 7.3% in Mg_3Sb_2/MgAgSb Module for Low-Temperature Energy Harvesting. *Joule* **2021**, *5* (5), 1196−1208.

(7) Petsagkourakis, I.; Tybrandt, K.; Crispin, X.; Ohkubo, I.; Satoh, N.; Mori, T. Thermoelectric Materials and Applications for Energy Harvesting Power Generation. *Sci. Technol. Adv. Mater.* **2018**, *19* (1), 836−862.

(8) Nandihalli, N.; Liu, C.-J.; Mori, T. Polymer Based Thermoelectric Nanocomposite Materials and Devices: Fabrication and Characteristics. *Nano Energy* **2020**, *78*, 105186.

(9) Soleimani, Z.; Zoras, S.; Ceranic, B.; Cui, Y.; Shahzad, S. A Comprehensive Review On the Output Voltage/Power of Wearable Thermoelectric Generators Concerning Their Geometry and Thermoelectric Materials. *Nano Energy* **2021**, *89*, 106325.

(10) Chen, Y.; He, M.; Liu, B.; Bazan, G. C.; Zhou, J.; Liang, Z. Bendable N-Type Metallic Nanocomposites With Large Thermoelectric Power Factor. *Adv. Mater.* **2017**, *29* (4), 1604752.

(11) Zhao, L. D.; Lo, S. H.; Zhang, Y.; Sun, H.; Tan, G.; Uher, C.; Wolverton, C.; Dravid, V. P.; Kanatzidis, M. G. Ultralow Thermal Conductivity and High Thermoelectric Figure of Merit in SnSe Crystals. *Nature* **2014**, *508* (7496), 373−377.

(12) Sootsman, J. R.; Chung, D. Y.; Kanatzidis, M. G. New and Old Concepts in Thermoelectric Materials. *Angew. Chem., Int. Ed.* **2009**, *48* (46), 8616−8639.

(13) Park, T.; Park, C.; Kim, B.; Shin, H.; Kim, E. Flexible PEDOT Electrodes with Large Thermoelectric Power Factors to Generate Electricity by the Touch of Fingertips. *Energy Environ. Sci.* **2013**, *6* (3), 788.

(14) Hong, C. T.; Lee, W.; Kang, Y. H.; Yoo, Y.; Ryu, J.; Cho, S. Y.; Jang, K.-S. Effective Doping by Spin-Coating and Enhanced Thermoelectric Power Factors in SWCNT/P3HT Hybrid Films. *J. Mater. Chem. A* **2015**, *3* (23), 12314−12319.

(15) Yao, Q.; Chen, L.; Zhang, W.; Liufu, S.; Chen, X. C. Enhanced Thermoelectric Performance of Single-Walled Carbon Nanotubes/Polyaniline Hybrid Nanocomposites. *ACS Nano* **2010**, *4* (4), 2445−2451.

(16) Kim, D.; Kim, Y.; Choi, K.; Grunlan, J. C.; Yu, C. Improved Thermoelectric Behavior of Nanotube-Filled Polymer Composites with Poly(3,4-ethylenedioxythiophene) Poly(styrenesulfonate). *ACS Nano* **2010**, *4*, 513−523.

(17) Park, D.; Kim, M.; Kim, J. Conductive PEDOT: PSS-Based Organic/Inorganic Flexible Thermoelectric Films and Power Generators. *Polymers* **2021**, *13* (2), 210.

(18) Du, F. P.; Cao, N. N.; Zhang, Y. F.; Fu, P.; Wu, Y. G.; Lin, Z. D.; Shi, R.; Amini, A.; Cheng, C. PEDOT:PSS/Graphene Quantum Dots Films with Enhanced Thermoelectric Properties Via Strong Interfacial Interaction and Phase Separation. *Sci. Rep.* **2018**, *8* (1), 6441.

(19) Yao, Q.; Chen, L.; Zhang, W.; Liufu, S.; Chen, X. Enhanced Thermoelectric Performance of Single-Walled Carbon Nanotubes/Polyaniline Hybrid Nanocomposites. *ACS Nano* **2010**, *4*, 2445.

(20) Kim, D.; Kim, Y.; Choi, K.; Grunlan, J. C.; Yu, C. Improved Thermoelectric Behavior of Nanotube-Filled Polymer Composites with Poly(3,4-ethylenedioxythiophene) Poly(styrenesulfonate). *ACS Nano* **2010**, *4*, 513.

(21) Liu, C.; Jiang, F.; Huang, M.; Lu, B.; Yue, R.; Xu, J. Free-Standing PEDOT-PSS/$Ca_3Co_4O_9$ Composite Films as Novel Thermoelectric Materials. *J. Electron. Mater.* **2011**, *40* (5), 948−952.

(22) Hata, S.; Taguchi, K.; Oshima, K.; Du, Y.; Shiraishi, Y.; Toshima, N. Preparation of Ga-ZnO Nanoparticles Using Microwave and Ultrasonic Irradiation, and the Application of Poly(3,4-ethyl-

enedioxythiophene)-poly(styrenesulfonate) Hybrid Thermoelectric Films. *ChemistrySelect* **2019**, *4* (22), 6800−6804.
(23) Jiang, C.; Ding, Y.; Cai, K.; Tong, L.; Lu, Y.; Zhao, W.; Wei, P. Ultrahigh Performance of N-Type Ag_2Se Films for Flexible Thermoelectric Power Generators. *ACS Appl. Mater. Interfaces* **2020**, *12* (8), 9646−9655.
(24) Choi, J.; Cho, K.; Yun, J.; Park, Y.; Yang, S.; Kim, S. Large Voltage Generation of Flexible Thermoelectric Nanocrystal Thin Films by Finger Contact. *Adv. Energy Mater.* **2017**, *7* (21), 1700972.
(25) Chen, X.; Feng, L.; Yu, P.; Liu, C.; Lan, J.; Lin, Y. H.; Yang, X. Flexible Thermoelectric Films Based on Bi_2Te_3 Nanosheets and Carbon Nanotube Network with High *N*-Type Performance. *ACS Appl. Mater. Interfaces* **2021**, *13* (4), 5451−5459.
(26) Gao, J.; Miao, L.; Liu, C.; Wang, X.; Peng, Y.; Wei, X.; Zhou, J.; Chen, Y.; Hashimoto, R.; Asaka, T.; Koumoto, K. A Novel Glass-Fiber-Aided Cold-Press Method for Fabrication of N-type Ag_2Te Nanowires Thermoelectric Film on Flexible Copy-Paper Substrate. *J. Mater. Chem. A* **2017**, *5* (47), 24740−24748.
(27) Lu, Z.; Zhang, H.; Mao, C.; Li, C. M. Silk Fabric-Based Wearable Thermoelectric Generator For energy Harvesting From the Human Body. *Appl. Energy* **2016**, *164*, 57−63.
(28) Wan, C.; Gu, X.; Dang, F.; Itoh, T.; Wang, Y.; Sasaki, H.; Kondo, M.; Koga, K.; Yabuki, K.; Snyder, G. J.; Yang, R.; Koumoto, K. Flexible N-type Thermoelectric Materials by Organic Intercalation of Layered Transition Metal Dichalcogenide TiS_2. *Nat. Mater.* **2015**, *14* (6), 622−627.
(29) Kim, N.; Kee, S.; Lee, S. H.; Lee, B. H.; Kahng, Y. H.; Jo, Y. R.; Kim, B. J.; Lee, K. Highly Conductive PEDOT:PSS Nanofibrils Induced by Solution-Processed Crystallization. *Adv. Mater.* **2014**, *26* (14), 2268−2272.
(30) Goo, G.; Anoop, G.; Unithrattil, S.; Kim, W. S.; Lee, H. J.; Kim, H. B.; Jung, M. H.; Park, J.; Ko, H. C.; Jo, J. Y. Proton - Irradiation Effects on the Thermoelectric Properties of Flexible Bi_2Te_3/PEDOT:PSS Composite Films. *Adv. Electron. Mater.* **2019**, *5* (4), 1800786.
(31) Lu, Y.; Qiu, Y.; Cai, K.; Li, X.; Gao, M.; Jiang, C.; He, J. Ultrahigh Performance PEDOT/Ag_2Se/CuAgSe Composite Film for Wearable Thermoelectric Power Generators. *Mater. Today Phys.* **2020**, *14*, 100223.
(32) Yan, Z.; Zhao, Y.; Liu, D.; Zhang, Z.; Zheng, Y.; Cui, J.; Zhang, Y.; Xue, C. Thermoelectric Properties of Flexible PEDOT:PSS - Based Films Tuned by SnSe Via the Vacuum Filtration Method. *RSC Adv.* **2020**, *10* (71), 43840−43846.
(33) Gueye, M. N.; Carella, A.; Faure-Vincent, J.; Demadrille, R.; Simonato, J.-P. Progress in Understanding Structure and Transport Properties of PEDOT-Based Materials: A critical review. *Prog. Mater. Sci.* **2020**, *108*, 100616.
(34) Lee, W.; Lee, S.; Kim, H.; Kim, Y. Organic Thermoelectric Devices with PEDOT:PSS/ZnO Hybrid Composites. *Chem. Eng. J.* **2021**, *415*, 128935.
(35) Meng, Q.; Song, H.; Du, Y.; Ding, Y.; Cai, K. Facile Preparation of Poly(3,4-ethylenedioxythiophene): poly(styrenesulfonate)/Ag_2Te Nanorod Composite Films for Flexible Thermoelectric Generator. *J. Materiomics* **2021**, *7* (2), 302−309.
(36) Tsujii, N.; Mori, T. High Thermoelectric Power Factor in A Carrier-Doped Magnetic Semiconductor $CuFeS_2$. *Appl. Phys. Express* **2013**, *6* (4), No. 043001.
(37) Ang, R.; Khan, A. U.; Tsujii, N.; Takai, K.; Nakamura, R.; Mori, T. Thermoelectricity Generation and Electron-Magnon Scattering in a Natural Chalcopyrite Mineral From a Deep-Sea Hydrothermal Vent. *Angew. Chem.* **2015**, *127* (44), 13101−13105.
(38) Tsujii, N.; Mori, T.; Isoda, Y. Phase Stability and Thermoelectric Properties of $CuFeS_2$-Based Magnetic Semiconductor. *J. Electron. Mater.* **2014**, *43* (6), 2371−2375.
(39) Li, Y.; Zhang, T.; Qin, Y.; Day, T.; Jeffrey Snyder, G.; Shi, X.; Chen, L. Thermoelectric Transport Properties of Diamond-Like $Cu_{1-x}Fe_{1+x}S_2$ Tetrahedral Compounds. *J. Appl. Phys.* **2014**, *116*, 203705.
(40) Liang, D.; Ma, R.; Jiao, S.; Pang, G.; Feng, S. A facile Synthetic Approach For Copper Iron Sulfide Nanocrystals with Enhanced Thermoelectric Performance. *Nanoscale* **2012**, *4* (20), 6265−6268.
(41) Yildirim, E.; Wu, G.; Yong, X.; Tan, T. L.; Zhu, Q.; Xu, J.; Ouyang, J.; Wang, J.-S.; Yang, S.-W. A Theoretical Mechanistic Study on Electrical Conductivity Enhancement of DMSO Treated PEDOT:PSS. *J. Mater. Chem. C* **2018**, *6* (19), 5122−5131.
(42) Ashcroft, N. W.; Mermin, N. D. In *Solid State Physics*; Cengage Learning: Boston, 1976; p 187.
(43) Bastola, E.; Bhandari, K. P.; Subedi, I.; Podraza, N. J.; Ellingson, R. J. Structural, Optical, and Hole Transport Properties of Earth-Abundant Chalcopyrite ($CuFeS_2$) Nanocrystals. *MRS Commun.* **2018**, *8* (3), 970−978.
(44) Hewidy, D.; Gadallah, A. S.; Fattah, G. A. Electroluminescence Enhancement of Glass/ITO/PEDOT:PSS/MEH-PPV/PEDOT:PSS/Al OLED by Thermal Annealing. *J. Mol. Struct.* **2017**, *1130*, 327−332.
(45) Zhang, D.; Ryu, K.; Liu, X.; Polikarpov, E.; Ly, J.; Tompson, M. E.; Zhou, C. Transparent, Conductive, and Flexible Carbon Nanotube Films and Their Application in Organic Light-Emitting Diodes. *Nano Lett.* **2006**, *6*, 1880.
(46) Wang, L.; Yao, Q.; Xiao, J.; Zeng, K.; Qu, S.; Shi, W.; Wang, Q.; Chen, L. Engineered Molecular Chain Ordering in Single-Walled Carbon Nanotubes/Polyaniline Composite Films for High-Performance Organic Thermoelectric Materials. *Chem. - Asian J.* **2016**, *11* (12), 1804−1810.
(47) Lu, Y.; Qiu, Y.; Cai, K.; Ding, Y.; Wang, M.; Jiang, C.; Yao, Q.; Huang, C.; Chen, L.; He, J. Ultrahigh Power Factor and Flexible Silver Selenide-Based Composite Film For Thermoelectric Devices. *Energy Environ. Sci.* **2020**, *13* (4), 1240−1249.
(48) Wei, J.; Wang, Y.; Li, X.; Jia, Z.; Qiao, S.; Zhang, Q.; Du, J. Effect of Porosity and Crack on the Thermoelectric Properties of Expanded Graphite/Carbon Fiber Reinforced Cement-Based Composites. *Int. J. Energy Res.* **2020**, *44* (8), 6885−6893.
(49) Chen, T.-H.; Chen, P.-H.; Chen, C.-H. Laser Co-Ablation of Bismuth Antimony Telluride and Diamond-Like Carbon Nanocomposites for Enhanced Thermoelectric Performance. *J. Mater. Chem. A* **2018**, *6* (3), 982−990.
(50) Jung, S. H.; Kim, K. T.; Lee, G. S.; Sun, J. Y.; Kim, D. W.; Eom, Y. S.; Yang, D. Y.; Yu, J.; Park, J. M.; Hyeon, D. Y.; Park, K. I. Synergistically Improved Thermoelectric Energy Harvesting of Edge-Oxidized-Graphene-Bridged N-Type Bismuth Telluride Thick Films. *ACS Appl. Mater. Interfaces* **2021**, *13* (4), 5125−5132.
(51) Cho, Y. M.; Kim, K. T.; Lee, G. S.; Kim, S. H. The Role of Edge-Oxidized Graphene to Improve the Thermopower of P-type Bismuth Telluride-Based Thick Films. *Appl. Surf. Sci.* **2019**, *476*, 533−538.
(52) Li, J. C.; Li, D.; Xu, W.; Qin, X. Y.; Li, Y. Y.; Zhang, J. Enhanced Thermoelectric Performance of SnSe Based Composites with Carbon Black Anoinclusions. *Appl. Phys. Lett.* **2016**, *109*, 173902.
(53) Sirringhaus, H.; Brown, P. J.; Friend, R. H.; Nielsen, M. M.; Bechgaard, K.; Langeveld-Voss, B. M. W.; Spiering, A. J. H.; Janssen, R. A. J.; Meijer, E. W.; Herwig, P.; de Leeuw, D. M. Two-Dimensional Charge Transport in Self-Organized, High Mobility Conjugated Polymers. *Nature* **1999**, *401*, 685−688.
(54) Park, C.; Yoo, D.; Im, S.; Kim, S.; Cho, W.; Ryu, J.; Kim, J. H. Large-Scalable RTCVD Graphene/PEDOT:PSS Hybrid Conductive Film for Application in Transparent and Flexible Thermoelectric Nanogenerators. *RSC Adv.* **2017**, *7* (41), 25237−25243.
(55) Yao, Y.; Dong, H.; Hu, W. Charge Transport in Organic and Polymeric Semiconductors for Flexible and Stretchable Devices. *Adv. Mater.* **2016**, *28* (22), 4513−4523.
(56) Huang, L.; Lu, J.; Ma, D.; Ma, C.; Zhang, B.; Wang, H.; Wang, G.; Gregory, D. H.; Zhou, X.; Han, G. Facile in Situ Solution Synthesis of SnSe/rGO Nanocomposites with Enhanced Thermoelectric Performance. *J. Mater. Chem. A* **2020**, *8* (3), 1394−1402.
(57) Shin, W. H.; Ahn, K.; Jeong, M.; Yoon, J. S.; Song, J. M.; Lee, S.; Seo, W. S.; Lim, Y. S. Enhanced Thermoelectric Performance of Reduced Graphene Oxide Incorporated Bismuth-Antimony-Telluride

https://doi.org/10.1021/acsami.1c15232
ACS Appl. Mater. Interfaces 2021, 13, 51245−51254

by Lattice Thermal Conductivity Reduction. *J. Alloys Compd.* **2017**, *718*, 342−348.
(58) Jagadish, P. R.; Khalid, M.; Li, L. P.; Amin, N.; Walvekar, R.; Chan, A. Effect of Graphene Doping on the Charge Carrier and Thermoelectric Properties of RCF-Bi_2S_3 Composites. *AIP Conf. Proc.* **2019**, *2137*, No. 020004.
(59) Amollo, T. A.; Mola, G. T.; Kirui, M. S. K.; Nyamori, V. O. Graphene for Thermoelectric Applications: Prospects and Challenges. *Crit. Rev. Solid State Mater. Sci.* **2018**, *43* (2), 133−157.
(60) Wang, L.; Yao, Q.; Bi, H.; Huang, F.; Wang, Q.; Chen, L. Large Thermoelectric Power Factor in Polyaniline/Graphene Nanocomposite Films Prepared by Solution-Assistant Dispersing Method. *J. Mater. Chem. A* **2014**, *2* (29), 11107.
(61) Li, X.; Yin, J.; Zhou, J.; Wang, Q.; Guo, W. Exceptional high Seebeck Coefficient and Gas-Flow-Induced Voltage in Multilayer Graphene. *Appl. Phys. Lett.* **2012**, *100*, 183108.
(62) Zhang, B.; Sun, J.; Katz, H. E.; Fang, F.; Opila, R. L. Promising Thermoelectric Properties of Commercial PEDOT:PSS Materials and Their Bi_2Te_3 Powder Composites. *ACS Appl. Mater. Interfaces* **2010**, *2* (11), 3170−3178.
(63) Piotrowski, M.; Franco, M.; Sousa, V.; Rodrigues, J.; Deepak, F. L.; Kakefuda, Y.; Kawamoto, N.; Baba, T.; Owens-Baird, B.; Alpuim, P.; Kovnir, K.; Mori, T.; Kolen'ko, Y. V. Probing of Thermal Transport in 50 nm Thick PbTe Nanocrystal Films by Time-Domain Thermoreflectance. *J. Phys. Chem. C* **2018**, *122* (48), 27127−27134.
(64) Liu, J.; Jia, Y.; Jiang, Q.; Jiang, F.; Li, C.; Wang, X.; Liu, P.; Liu, P.; Hu, F.; Du, Y.; Xu, J. Highly Conductive Hydrogel Polymer Fibers toward Promising Wearable Thermoelectric Energy Harvesting. *ACS Appl. Mater. Interfaces* **2018**, *10* (50), 44033−44040.
(65) Mallick, M. M.; Rosch, A. G.; Franke, L.; Ahmed, S.; Gall, A.; Gesswein, H.; Aghassi, J.; Lemmer, U. High-Performance Ag-Se-Based n-Type Printed Thermoelectric Materials for High Power Density Folded Generators. *ACS Appl. Mater. Interfaces* **2020**, *12* (17), 19655−19663.
(66) Chen, Y.; He, M.; Tang, J.; Bazan, G. C.; Liang, Z. Flexible Thermoelectric Generators with Ultrahigh Output Power Enabled by Magnetic Field-Aligned Metallic Nanowires. *Adv. Electron. Mater.* **2018**, *4* (9), 1800200.
(67) Tian, R.; Wan, C.; Wang, Y.; Wei, Q.; Ishida, T.; Yamamoto, A.; Tsuruta, A.; Shin, W.; Li, S.; Koumoto, K. A Solution-Processed TiS_2/Organic Hybrid Superlattice Film Towards Flexible Thermoelectric Devices. *J. Mater. Chem. A* **2017**, *5* (2), 564−570.
(68) Oh, J. Y.; Lee, J. H.; Han, S. W.; Chae, S. S.; Bae, E. J.; Kang, Y. H.; Choi, W. J.; Cho, S. Y.; Lee, J.-O.; Baik, H. K.; Lee, T. I. Chemically Exfoliated Transition Metal Dichalcogenide Nanosheet-Based Wearable Thermoelectric Generators. *Energy Environ. Sci.* **2016**, *9* (5), 1696−1705.
(69) Wan, C.; Tian, R.; Azizi, A. B.; Huang, Y.; Wei, Q.; Sasai, R.; Wasusate, S.; Ishida, T.; Koumoto, K. Flexible Thermoelectric Foil for Wearable Energy Harvesting. *Nano Energy* **2016**, *30*, 840−845.

https://doi.org/10.1021/acsami.1c15232
ACS Appl. Mater. Interfaces 2021, 13, 51245−51254